Research Square

Preprints are preliminary reports that have not undergone peer review.
They should not be considered conclusive, used to inform clinical practice,
or referenced by the media as validated information.

Acoustic Analysis Comparison and Model Optimization of Chinese Ancient and Modern Oboes

Yuanyuan Niu
Shanxi University
Peng Peng
pengpeng@sxu.edu.cn
Shanxi University
Zhenghui Jia
Shanxi University
Zilong Niu
Jinzhong College of Information
Jiayun Wang
North University of China

Article

Keywords: Suona, Sunaiyi, acoustic characteristics, Finite element simulation, model optimization

Posted Date: July 27th, 2026

DOI: https://doi.org/10.21203/rs.3.rs-10197806/v1

License: This work is licensed under a Creative Commons Attribution 4.0 International License.
Read Full License

Additional Declarations: No competing interests reported.

Version of Record: A version of this preprint was published at Scientific Reports on October 29th, 2026.
See the published version at https://doi.org/10.1038/s41598-026-77157-6.

Acoustic Analysis Comparison and Model Optimization of Chinese Ancient and Modern Oboes

YuanYuan Niu [1,2], Peng Peng [1,*], Zhenghui Jia [3], Zilong Niu [4], Jiayun Wang [5,*]

[1]Institute for History of Science and Technology, Shanxi University, Taiyuan 030006, China

[2]Shanxi Polytechnic College, Taiyuan 030006, China

[3]The Academy of Music, Shanxi University, Taiyuan 030006, China

[4]Jinzhong College of Information, Taiyuan 030800, China

[5]State key Laboratory of Extreme Environment Optoelectronic Dynamic Measurement Technology and Instrument, North University of China,030051, Shanxi Taiyuan, China

*corresponding. pengpeng@sxu.edu.cn, wangjiayun@nuc.edu.cn

Abstract:

As a traditional Chinese double-reed woodwind instrument, the Suona has evolved through representative forms such as the Tang Bili and Qing Sunaiyi. However, systematic studies on its acoustic characteristics across historical evolution remain scarce. This work takes the Qing Sunaiyi and the modern standard Suona as samples, and adopts an integrated approach combining three-dimensional scanning, finite element simulation, and intelligent optimization. High-fidelity axisymmetric finite element models are built based on historical records and scanning data. The two instruments are compared in far-field sound pressure level, directivity, central-axis pressure distribution, and internal sound field, followed by parametric optimization of the modern Suona bell profile. Results show that the Sunaiyi has a longer tube and gentler bell flare, leading to higher overtone frequencies and unstable high-order overtones. In contrast, the modern Suona, with a shorter tube and steeper bell flare, achieves a lower fundamental overtone, smoother far-field attenuation, and more concentrated directivity. Spectral measurements in a professional studio agree well with simulations, validating the numerical models. A surrogate-assisted K-means clustering particle swarm optimization algorithm with diversity control (SAPSO-BCM) is proposed and coupled with COMSOL for global optimization of bell curvature to maximize far-field sound pressure level. This work pioneers the integrated three-dimensional scanning, FEM, and intelligent optimization workflow for Suona acoustics, quantifying the influence of bell geometry on radiation performance and offering a generalizable engineering method for traditional wind instruments.

Key words: Suona, Sunaiyi, acoustic characteristics, Finite element simulation, model optimization

Introduction

As a double-reed aerophone widely employed in traditional Chinese folk music genres such as wind-and-percussion ensembles and BAYIN instrumental groups, the Suona is renowned for its resonant, penetrating timbre. From an acoustic engineering perspective, its sound pressure level and directional radiation characteristics are governed by geometric features, body materials and the contour of the terminal bell. In particular, the brass bell serves as a critical impedance matching component at the tube end, which largely determines acoustic radiation efficiency and far-field directivity patterns. Accordingly, quantitatively comparing the acoustic performance of Qing-dynasty sunayi and modern Suonas via modern acoustic engineering approaches, and exploring how the evolution of bell profiles affects sound radiation

mechanisms, carries significant academic implications. Traditional instrument shaping has long relied on craftsmen's experience, lacking quantitative optimization frameworks built on physical models. In recent years, advances in computational acoustics and optimization algorithms have made finite element-based acoustic optimization for musical instruments feasible [1-3]. A systematic comparative acoustic analysis and geometric optimization targeting Qing-dynasty Sunaiyi and modern Suonas can not only establish theoretical support for the scientific design of Suonas, but also provide technical references for the acoustic improvement of other traditional double-reed instruments.

With the advancement of modern technologies, researchers have increasingly combined numerical simulation and experimental testing to clarify correlations between the acoustic properties and structural parameters of musical instruments. Popular technical approaches include computational fluid dynamics (CFD) coupled simulation [4-8], X-ray CT alongside archaeological characterization techniques [9-14], numerical continuation and bifurcation analysis [15-17], as well as finite element-based numerical modeling [18-23]. CFD methods solve the Navier-Stokes equations to reproduce the nonlinear interaction between airflow jets and resonant cavities, and adopt spectral analysis to distinguish flow patterns at different frequencies, thereby clarifying the interplay between blowing pressure, reed vibration and sound fields. For instance, Yoshinaga and col-leagues conducted aero acoustic simulations on the mouthpiece and resonator of single-reed instruments by coupling one-dimensional and two-dimensional reed deformation models, and examined how two-dimensional reed oscillation alters airflow and sound generation [6]. Adachi proposed a jet oscillation model for flute-type instruments, which accurately reproduced the head joint reflection coefficient and analyzed the acoustic responses under varying tube lengths [7]. X-ray CT enables non-destructive re-construction of three-dimensional internal structures of musical instruments, offering solid technical support for investigating manufacturing techniques, material selection and acoustic design concepts. Francesca's team carried out CT scanning on a recorder and a Baroque transverse flute, extracting information related to craftsmanship, material properties, preservation conditions and historical repairs to evaluate the structural traits of woodwind instruments [9]. Festa and co-workers adopted neutron-based testing to analyze a metal flute from the 19th century, characterizing its crystal structure and elemental composition to compare material properties of flutes from different eras [13].

As a mature technical tool, the finite element method (FEM)discretizes instrument geometries and solves partial differential equations describing elastic vibration and acoustic coupling, and has been widely applied to explore the vibro-acoustic behaviors of musical instruments. Brezas and his research group integrated modal testing, combined finite element and boundary element simulation, and sound field characterization to verify the potential of alternative materials in enhancing structural durability, reducing overall weight and regulating vibration modes of musical instruments [20]. Sabin adopted finite element modeling to analyze the structural mechanics of free-reed instruments, and validated the relationship between blowing pressure and fundamental frequency through physical experiments [22]. Despite the extensive application of finite element simulation in acoustic research on various musical instruments, quantitative comparative studies focusing on the acoustic performance of Chinese Suonas, especially ancient sunayi and modern counterparts, remain scarce. Most existing works focus on ethnomusicological documentation or basic acoustic measurement, while systematic discussions on how geometric differences across historical periods transform sound radiation performance are still lacking. Meanwhile, the influence of bell geometry on the far-field sound pressure level and directivity of wind instruments has drawn growing research attention. Takayama et al. adopted the boundary element method to discuss how flare angles impact the sound radiation of brass instrument bells [24]. Chen's team optimized the bell contour of saxophones using the

finite element method and successfully raised the sound pressure level within designated frequency bands [25]. Nevertheless, these studies mainly target Western wind instruments, and few efforts have extended such methods to the bell optimization of Chinese Suonas.

To fill the above research gaps, this study takes Qing-dynasty sunayi and modern Suonas as research subjects. First, three-dimensional scanning is adopted to acquire precise geometric models of the two types of instruments, and high-fidelity finite element simulation models are established. Under identical excitation conditions, the internal sound pressure distribution, far-field sound pressure level and radiation directivity of the two instruments are compared, so as to quantitatively assess how bell geometry affects acoustic radiation efficiency. On this basis, a surrogate-assisted improved particle swarm optimization algorithm (SAPSO-BCM) is introduced. With the objective of maximizing the far-field sound pressure level within target frequency bands, parametric shape optimization is performed on bell contours. Acoustic performance before and after optimization is further compared to verify the effectiveness of the proposed algorithm. This work pioneers the application of a complete technical framework combining three-dimensional scanning, finite element simulation and intelligent optimization algorithms to the acoustic analysis of Suonas. It clarifies the quantitative relationship between bell shapes and sound radiation characteristics, and provides reusable engineering strategies for the scientific design and performance improvement of traditional wind instruments.

Results and discussions

Acoustic Analysis via Numerical Simulation

Based on the finite element models and simulation settings for the Qing-dynasty Sunaiyi and the modern Suona, which were established from historical records and 3D scanning data, the resulting models are illustrated in Figure 1. This chapter presents a systematic comparative analysis and optimization validation of the acoustic characteristics of the two instruments from both numerical simulation and experimental testing perspectives. Through finite element simulations, the far-field sound pressure level, external field directivity, sound pressure distribution along the central axis, and the influence of different materials were analyzed to quantitatively evaluate the radiation performance of the two instruments under identical excitation conditions. The far-field sound pressure level as a function of distance from the bell exit for the three partials of the Qing-dynasty Sunaiyi and modern Suona during performance is shown in Figure 2. The abscissa represents the distance from the bell. From Figure 2(a), it can be observed that for Sunaiyi, the sound pressure levels corresponding to the three partials all exhibit a decaying trend with increasing distance. The first partial has the highest sound pressure level at the bell exit, followed by the second partial, and the third partial the lowest, with frequencies of 942 Hz, 1880 Hz, and 2840 Hz, respectively. During the decay process, the curve of the third partial shows pronounced fluctuations, reflecting the poorer stability of higher-order partials during propagation. In comparison, for the modern Suona shown in Figure 2(b), the spectral positions of its three partials are generally lower than those of Sunaiyi, and at each distance the sound pressure levels are higher than those of the corresponding partials of Sunaiyi. Moreover, the decay curve of the third partial of the modern Suona is smoother, with significantly reduced fluctuations, indicating better radiation stability of its higher-order partials. These differences suggest that owing to its longer tube length and gentler bell flare curve, Sunaiyi exhibits higher resonance frequencies and lower acoustic impedance matching efficiency; by contrast, the modern Suona, with its shorter tube length and larger bell flare angle, facilitates efficient radiation of low-frequency energy while the copper material enhances the retention of far-field sound pressure level.

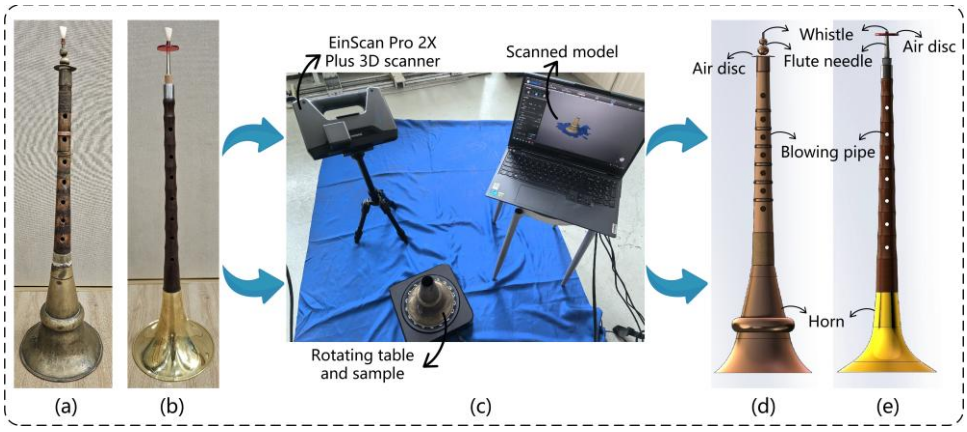


Figure 1. 3D scanning models and COMSOL co-simulation models: (a) and (b) Sunaiyi and Suona samples; (c) 3D scanning scene; (d) and (e) Sunaiyi and Suona simulation models.

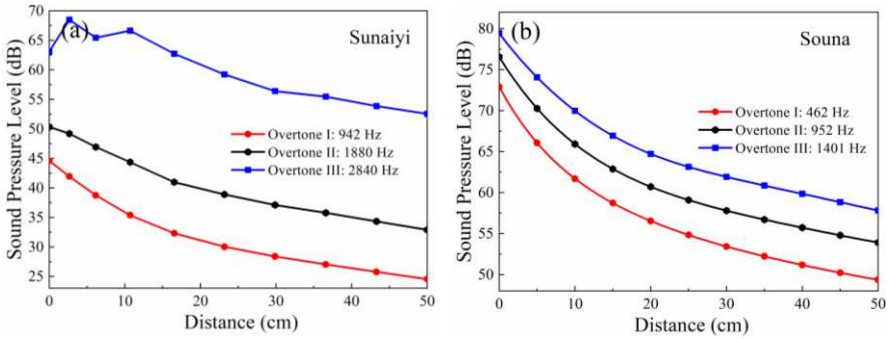


Figure 2. Far-field sound pressure level (a) Sunaiyi; (b) Souna.

Figure 3 illustrates the far-field acoustic characteristics of the Qing dynasty Sunaiyi and the modern Suona, where Figures 3a and b show the far-field sound pressure level directivity patterns of the two instruments, respectively, and Figures 3c and d present the corresponding far-field pressure directivity patterns. As can be seen from Figure 3a, the sound pressure level directivity of Sunaiyi at the first and second partials is relatively stable, with the main lobe concentrated in the 0° direction and only a narrow side lobe appearing at approximately 90°. When it comes to the third partial, the complexity of the directivity pattern increases significantly, exhibiting three side lobes located at about 72°, 90°, and 108°. This indicates that the bell shape of Sunaiyi has limited capability to control the diffraction of higher-order harmonics, resulting in energy leakage toward multiple lateral directions. In contrast, for the modern Suona shown in Figure 3b, the directivity at the first and second partials is more uniform, with small fluctuations in sound pressure level over the entire range of 0°-180°, demonstrating good omnidirectional stability. Its third partial also generates a side lobe near 90°, but with fewer side lobes than Sunaiyi, and the main lobe energy remains concentrated in the forward direction. This difference is attributed to the steeper flare curve and larger terminal curl of the modern Suona bell, which more effectively confine the energy of higher-order harmonics to the main lobe direction and reduce undesired lateral radiation.

The pressure directivity pattern of Sunaiyi in Figure 3c shows that the pressure value is highest in the forward direction within 0°-30°, while at other angles the pressure decays rapidly, accompanied by multiple side lobes. As the partial order increases, the number of side lobes grows; notably, in the pressure directivity pattern of the third partial, two nearly equal main lobes appear. This phenomenon may be attributed to the

fact that when high-frequency sound waves propagate through the long conical tube of Sunaiyi, non-axisymmetric high-order transverse resonance modes are excited, and the radiation patterns of these modes bifurcate along the axial direction, thereby forming a double-main-lobe structure. In Figure 3d, the pressure directivity of the modern Suona is significantly improved: the pressure remains high and stable within 0°-60°, with very few side lobes, and only a side lobe near 90° exists for the third partial. This indicates that the geometric optimization of the bell of the modern Suona weakens the excitation intensity of high-order transverse modes, concentrating the radiated energy more in the forward broad-angle region. Thus, the difference in far-field directivity between Sunaiyi and the modern Suona mainly arises from the evolution of the bell shape. Sunaiyi features a gentler bell flare, which is equivalent to a longer exponential horn; it provides good directivity for mid-to-high frequency sound waves but is prone to exciting high-order side lobes. In contrast, the modern Suona adopts a shorter bell with a larger flare angle, which enhances the impedance matching bandwidth and suppresses energy radiation in off-main-lobe directions, thereby achieving more stable and concentrated far-field directivity characteristics.

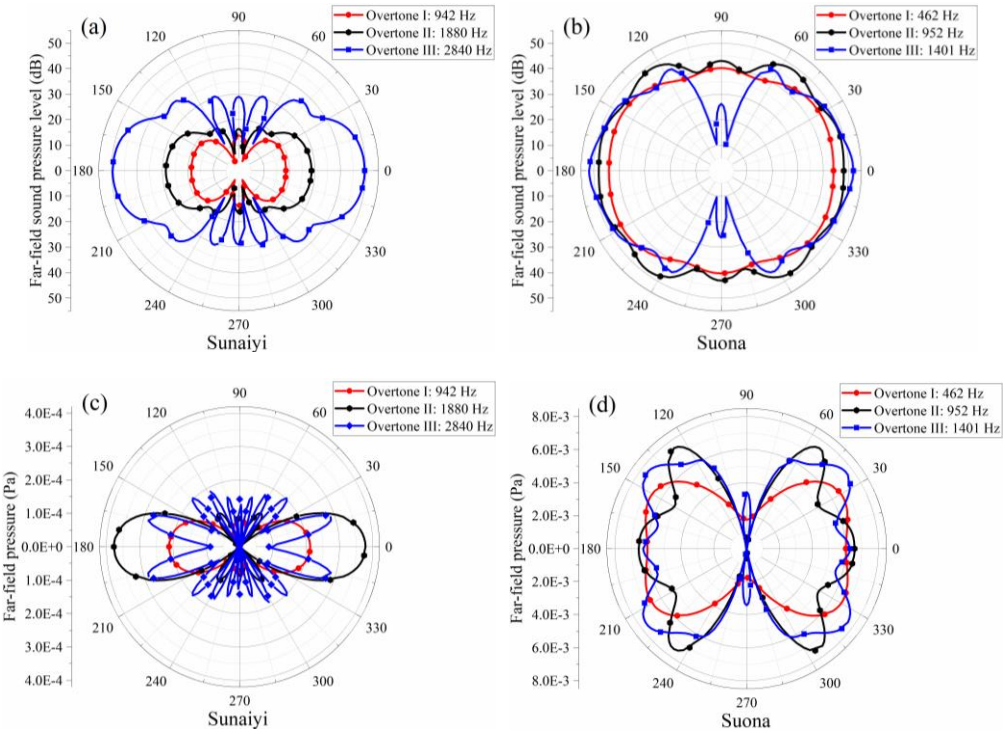


Figure 3. Far-field sound pressure level directivity patterns: (a) Sunaiyi and (b) Suona; far-field pressure directivity patterns: (c) Sunaiyi and (d) Suona.

Figure 4 presents the sound pressure level distribution along the central axis of the tube for the Qing dynasty Sunaiyi and the modern Suona, with the abscissa representing the distance from the bell exit. As shown in Figure 4a, the sound pressure level of Sunaiyi drops sharply at approximately 4 cm from the bell exit, with a decrease of 30-40 dB. This phenomenon can be attributed to the sudden change in acoustic impedance near the bell exit: when sound waves radiate outward from the tube opening, the edge diffraction effect and near-field interference create a strong sound pressure cancellation region, leading to a local steep drop in sound pressure. In the range of 4-50 cm, the sound pressure level tends to be relatively stable, fluctuating by approximately ±5 dB, indicating that this region is the transition zone from the near field to the far field, where a stable propagation pattern is gradually established. In the range of 50-100 cm, the sound pressure

level gradually decreases, consistent with the natural decay law of spherical wave diffusion. In comparison, as shown in Figure 4b, the modern Suona remains relatively stable over the range of 0-55 cm, with only a sudden drop of about 15 dB occurring for the first partial at approximately 8.5 cm from the bell exit, after which it quickly returns to normal levels. This sudden drop also originates from near-field interference at the tube opening, but thanks to the steeper flare curve and larger terminal curl of the modern Suona bell, the interference depth is effectively suppressed, making the drop much smaller than that of Sunaiyi. It is worth noting that, apart from this local drop, the fluctuation amplitude of the sound pressure level of the modern Suona within the 0-55 cm range is larger than that of Sunaiyi. This indicates that the impedance matching of the modern Suona bell design is still deficient and has considerable room for improvement; therefore, the optimization of the bell will be performed in the following section.

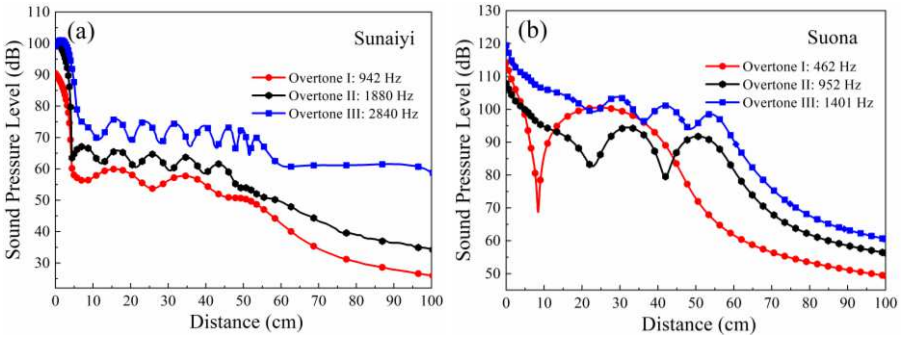


Figure 4. Far-field sound pressure level directivity patterns: (a) Sunaiyi and (b) Suona; far-field pressure directivity patterns: (c) Sunaiyi and (d) Suona.

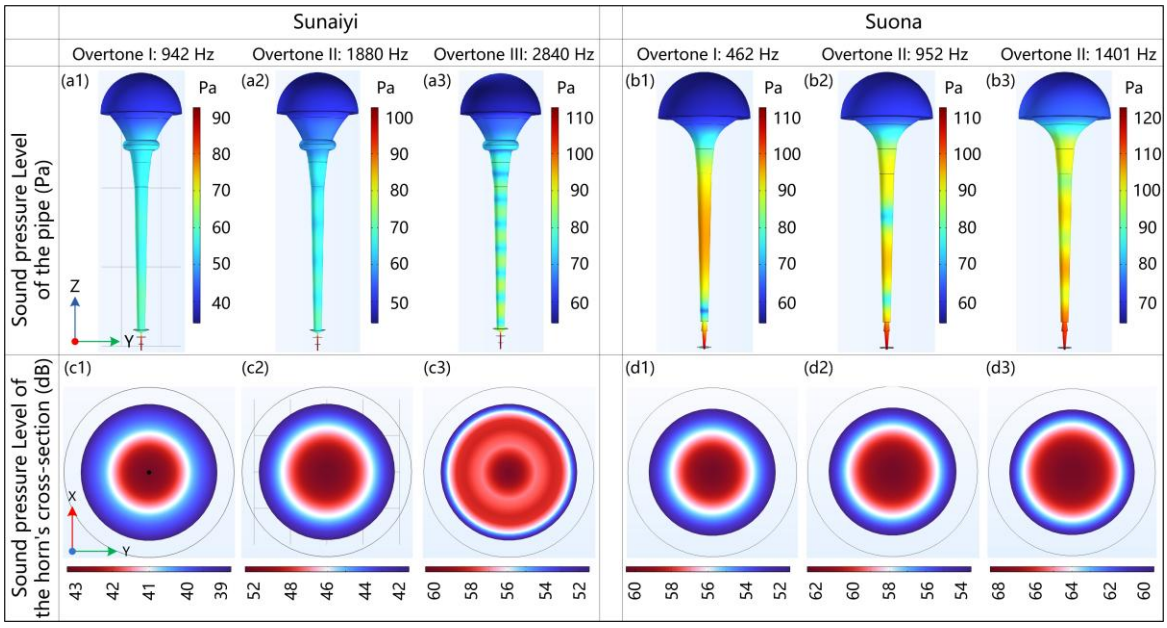


Figure 5. Sound pressure level field maps at the first, second, and third partials: (a) and (b) are field maps of the tube body for Sunaiyi and Suona, respectively; (c) and (d) are field maps of the bell cross-section for Sunaiyi and Suona, respectively.

Figure 5 shows the sound pressure level field distributions of Sunaiyi and Suona at different partials. From the longitudinal cross-sectional field maps of the tube interior (Figures 5a1–7a3), it can be seen that the

number of sound pressure peaks in Sunaiyi in-creases regularly with the order of the partial: three peaks appear at the first partial, five at the second, and seven at the third. This phenomenon conforms to the standing wave pattern characteristic of higher-order harmonics in an open-ended tube instrument, where the number of pressure antinodes inside the tube is proportional to the harmonic order. Owing to its longer tube length (45.25 cm) and smaller taper, Sunaiyi is closer to an ideal straight tube; consequently, the standing wave nodes of higher-order modes are clearly defined, and the number of peaks corresponds strictly to the harmonic order. In contrast, from Figures 5b1–5b3, the number of sound pressure peaks inside the modern Suona tube is significantly reduced: only one peak at the first partial, two at the second, and three at the third. This difference is mainly attributed to the more pronounced conical tube shape and larger expansion ratio of the bell in the modern Suona. The taper enhances the traveling wave component of sound waves propagating along the tube axis, weakens the formation of pure standing waves, makes the pressure distribution inside the tube more uniform, and thus reduces the number of standing wave peaks. At the same time, the strong acoustic impedance matching at the bell end promotes rapid outward radiation of energy, further suppressing the standing wave structure formed by multiple internal re-flections.

From the sound pressure distributions at the bell cross-section (Figures 5c1–5c3), the energy of the first and second partials of Sunaiyi is concentrated near the central region close to the axis, while at the third partial, the sound pressure spreads considerably to-ward the periphery, nearly reaching the inner wall of the bell. This indicates that the higher-order partial excites high-order transverse modes at the tube opening cross-section, causing acoustic energy to diffuse toward the edges and reducing the directivity of axial radiation. In contrast, for the modern Suona (Figures 5d1–7d3), the cross-sectional sound pressures of all partials are more concentrated near the central axis; especially at the third partial, the acoustic energy is significantly more focused than that of Sunaiyi, with no obvious edge diffusion. This is attributed to the steeper flare curve of the modern Suona bell, which effectively suppresses the excitation of high-order transverse modes and al-lows sound waves to be emitted from the tube opening as quasi-plane waves, thereby achieving better forward focusing capability. Therefore, the differences in sound pressure field distribution between the Qing dynasty Sunaiyi and the modern Suona essentially result from the combined effects of tube taper, bell flare curve, and terminal impedance matching. Through more scientific geometric design, the modern Suona significantly simplifies the standing wave pattern inside the tube and improves the uniformity of cross-sectional energy distribution, thus achieving more concentrated and efficient acoustic radiation performance.

The effects of tube material, wall thickness d, and bore diameter w on the sound pressure level and frequency of the second and third partials are investigated using the geometric model of the modern Suona as a baseline, as shown in Figure 6. From Figures 6a and 6b, it can be seen that for both bone and bamboo tube bodies, the sound pressure levels of the second and third partials do not change significantly with varying wall thickness. This indicates that, under the present simulation conditions, the absorption and scattering effects of the wall thickness on the sound field inside the tube are negligible within a certain range, and the tube wall has sufficient rigidity to withstand acoustic excitation without generating additional structural vibration losses. Therefore, wall thickness is not a critical factor affecting sound pressure level. From Figures 6c and 6d, it is evident that the bore diameter has a significant influence on the partial frequencies: as the bore diameter increases, the center frequencies of both the second and third partials shift toward lower frequencies. This phenomenon can be explained by the fact that increasing the bore diameter effectively enlarges the transverse scale of the air column inside the tube, allowing the air column to establish effective resonant coupling with longer-wavelength sound waves, thereby lowering the cutoff

frequencies of the various harmonics. Furthermore, a notable difference is observed between different materials: the sound pressure level of the bam-boo tube body is lower than that of the ebony tube body. This difference mainly arises from the discrepancy in sound velocity between the materials, with bamboo and wood having sound velocities of approximately 2380 m/s and 3600 m/s, respectively. The higher sound velocity enhances the reflection efficiency and resonance intensity of the tube wall on the sound waves inside the tube, while also improving the high-frequency harmonic structure, thus endowing the wooden tube body with higher sound pressure levels and a richer timbre. For the modern Suona, wall thickness has little effect on sound pressure level within the conventional processing range, whereas bore diameter is a key geometric parameter for controlling the instrument's pitch. Regarding materials, those with a higher sound velocity can significantly improve the loudness and high-frequency response capability of the instrument.

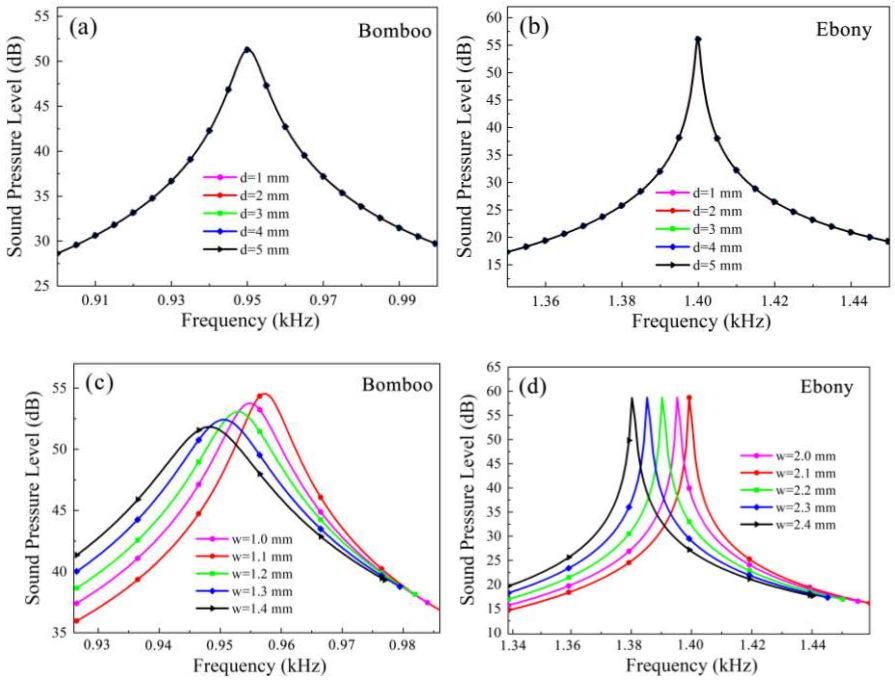


Figure 6. Sound pressure levels of Suona under different materials and dimensions: (a) and (b) data for different wall thicknesses; (c) and (d) data for different bore diameters.

Instrument Testing and Bell Model Optimization

To further verify the reliability of the finite element simulation results, actual performance recordings and spectral analyses of the Qing dynasty Sunaiyi and the modern Suona were conducted in a professional recording studio, GuideTone Studio, as shown in Figures 7 and 8. The measured results are as follows: for the Qing dynasty Sunaiyi, the center frequencies of the first five partials are 942 Hz, 1880 Hz, 2840 Hz, 3837 Hz, and 4822 Hz, with corresponding sound pressure levels of -23.6 dB, -27.6 dB, -30.1 dB, -38.2 dB, and -49.1 dB, respectively, as shown in Figure 8a. For the modern Suona, the frequencies of the first five partials are 462 Hz, 952 Hz, 1401 Hz, 1852 Hz, and 2312 Hz, with corresponding sound pressure levels of -49.8 dB, -31.2 dB, -17.1 dB, -27.7 dB, and -23.8 dB, respectively, as shown in Figure 8b. Comparing the measured data with the simulation results presented earlier, the partial frequency distributions and the decaying trend of sound pressure level with distance are in good agreement with the simulation results, thereby validating the accuracy of the finite element models.

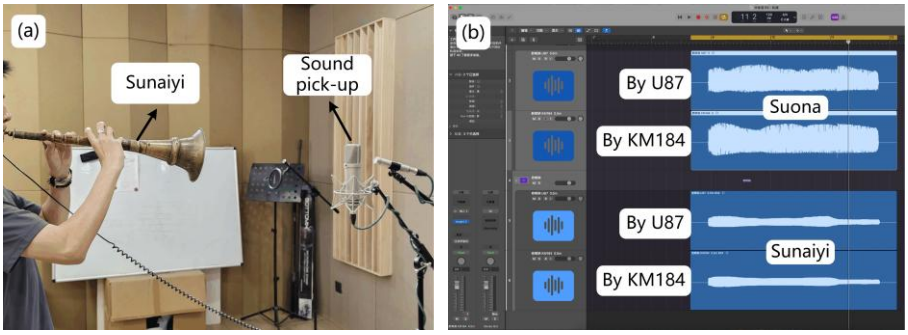


Figure 7. (a) Test site photograph; (b) Acquired sound spectrum.



Figure 8. Test data analysis: (a) Sunaiyi; (b) Suona.

Comparison of the measured spectral characteristics of the two instruments reveals that the sound pressure level of Sunaiyi exhibits a monotonic decreasing trend as the partial order increases, dropping from -23.6 dB at the first partial to -49.1 dB at the fifth partial, a decrease of 25.5 dB. This indicates that the acoustic energy of Sunaiyi is mainly concentrated in the fundamental frequency and lower-order harmonics, with significant attenuation of higher-order harmonic energy. In contrast, the sound pressure level of the modern Suona shows little fluctuation between the second and fifth partials, without monotonic attenuation; the third partial even becomes the strongest energy component (-17.1 dB). This difference is attributed to the bell shape optimization and tube taper de-sign of the modern Suona: the steeper bell flare curve and shorter tube length effectively adjust the impedance matching at the tube opening, significantly improving the radiation efficiency of harmonics in the specific mid-to-high frequency range (approximately 1.4-2.3 kHz), thereby suppressing the rapid attenuation of higher-order partials and resulting in a richer, brighter, and more balanced timbre. By contrast, the long conical tube and gentle flare design of Sunaiyi lead to poor acoustic impedance matching for higher-order harmonics, causing acoustic energy to dissipate rapidly as frequency increases. Therefore, the experimental test results not only verify the reliability of the simulations but also further quantify the essential differences in spectral envelope between the Qing dynasty Sunaiyi and the modern Suona, revealing the regulatory effect of bell and tube geometry evolution on harmonic energy distribution.

Furthermore, the modern Suona was subjected to optimization. In the process of optimizing the head curvature radius R of the Suona, to address the issues of traditional optimization algorithms easily falling into local optima and the high computational cost of COMSOL simulations [26], this paper proposes a diversity-controlled surrogate-assisted K-means clustering particle swarm optimization algorithm (SAPSO-BCM). A joint simulation and optimization framework combining the algorithm model with

COMSOL is constructed, achieving efficient global optimization of the head curvature radius R of the Suona and ultimately obtaining the Suona structure with optimal sound pressure level performance [27–28].The chaotic resetting mechanism introduced in this study can restore population diversity more efficiently than traditional random resetting, effectively suppressing premature convergence of the algorithm, avoiding the optimization process from falling into locally optimal curvature values, and improving the reliability of the global optimal solution. The complete workflow of the joint simulation of the SAPSO-BCM algorithm with COMSOL mainly includes the following stages: in the initialization stage, initial curvature samples are generated by LHS, COMSOL is called to perform real sound pressure level simulations, and the initial GP surrogate model is constructed; in the iterative optimization stage, within the evaluation budget, at each generation the four modules of SAPSO-BCM perform sub-swarm evolution, model management, and diversity control, and the record of the optimal curvature is updated; in the local refinement stage, when the evaluation budget is exhausted, the current optimal curvature value is used as the initial point, and Nelder-Mead local search is employed for further refinement; in the output stage, the curvature parameter of the Suona cavity that yields the optimal sound pressure level performance is finally obtained, and the optimal Suona structure model is output.

Through the synergistic action of its four modules, the SAPSO-BCM algorithm achieves low-cost surrogate-assisted evolution, adaptive model correction, and dynamic diversity maintenance. Its integration with COMSOL simulations ensures the accuracy of sound pressure level evaluation while greatly improving optimization efficiency, providing a reliable solution for the efficient global optimization of the Suona cavity curvature. Based on the proposed SAPSO-BCM algorithm framework and the joint COMSOL acoustic simulation optimization system, global optimization experiments under multiple sound pressure level targets were carried out for the head curvature radius R of the Suona. Experiments were conducted for five groups of different sound pressure levels: 20.1 dB, 30.5 dB, 37.5 dB, 51.9 dB, and 52.7 dB. The experimental results are shown in Figure 9.

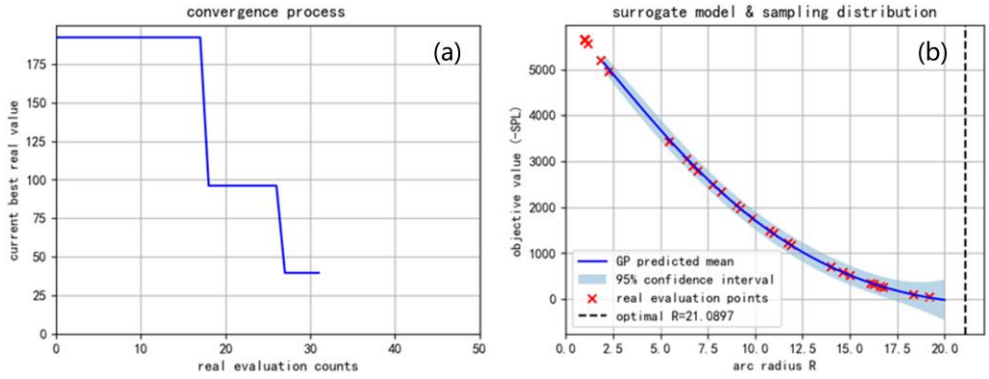


Figure 9. (a) Convergence process; (b) Surrogate model and sampling distribution

The experimental results show that in the early iteration stage of the optimization, K-means clustering enables the sub-swarms to explore the parameter space in parallel, and the LCB gradient guidance term quickly drives the particles toward high-potential regions. The fitness value decreases significantly within the first 20% of the iterations, and the convergence rate is markedly better than that of traditional PSO. In the middle iteration stage, periodic model management corrects the GP surrogate model bias in real time, elite opposition-based learning expands the neighborhood of high-quality solutions, and the population maintains a steady downward trend without falling into local optima traps. In the later iteration stage, the

chaotic diversity control module triggers resetting when population diversity falls below the threshold, effectively suppressing premature convergence, and the curve continues to approach the optimum smoothly. At the termination stage, after the evaluation budget is exhausted and Nelder-Mead local search re-fines the solution, all sound pressure level targets converge stably within a limited number of iterations, with the final fitness value fluctuation being less than 1%, indicating good optimization consistency.

During the optimization process, the SAPSO-BCM algorithm exhibits fast and smooth convergence, no severe oscillations, and no premature stagnation. The synergistic effects of LCB gradient guidance, chaotic diversity resetting, and periodic model management fundamentally overcome the shortcomings of traditional PSO, which are prone to premature convergence and unstable convergence, ensuring that the algorithm possesses reliable global convergence capability under multiple sound pressure level targets. Furthermore, based on the SAPSO-BCM algorithm and the COMSOL joint simulation framework, the optimal values of the Suona head curvature radius R under different target sound pressure levels were obtained experimentally, as shown in Table 1.

Table 1. Correspondence between different target sound pressure levels and optimal curvature radius values.

Target sound pressure level (dB)	Optimal curvature radius R (cm)
20.1	22.1
30.5	21.1
37.5	20.7
51.9	20.6
52.7	21.0

From the table, it can be seen that as the target sound pressure level increases, the optimal curvature generally shows a decreasing trend, but rebounds at extremely high sound pressure levels (52.7 dB). This nonlinear change indicates that the influence of the Suona head curvature on the sound pressure level output is not monotonic but involves a complex acoustic coupling mechanism. When the target sound pressure is low (20.1-30.5 dB), a larger curvature (21.1-22.1 cm) facilitates smooth propagation of acoustic energy; when the target sound pressure rises to 37.5-51.9 dB, a smaller curvature (20.6-20.7 cm) helps enhance sound radiation efficiency; however, when the sound pressure level further increases to around 52.7 dB, the system may enter a nonlinear acoustic region, where a larger curvature again becomes the better choice to suppress harmonic distortion or flow separation effects. This result provides a quantitative basis for the adaptive design of Suona structures under multiple operating conditions. In practical manufacturing, the corresponding optimal curvature or a value close to it can be selected according to the desired sound pressure level range for performance.

Conclusions

This study investigates the Qing-Dynasty Sunaiyi and modern Suona by combining three-dimensional scanning, FEM, experimental testing and surrogate-based intelligent optimization algorithms, and systematically clarifies their differences in acoustic performance as well as the regulating mechanism of bell geometry on sound radiation. Both simulation and experimental results indicate that the Sunaiyi possesses a longer tube and a gently flared bell, resulting in elevated overtone frequencies, poor stability of high-order harmonics, and obvious abrupt drop of sound pressure near the central axis in the near field. Benefiting from its shorter tube and steeper bell flare, the modern Suona delivers a lower fundamental

overtone frequency, smoother far-field attenuation and more focused sound directivity. Furthermore, the proposed SAPSO-BCM algorithm is combined with the COMSOL co-simulation framework to realize efficient global optimization of Suona bell curvature. The algorithm converges steadily, and the optimal curvature varies nonlinearly with the target sound pressure level within the range of 20.6 cm to 22.1 cm, which reflects the complex acoustic coupling between bell curvature and sound pressure level. This research is pioneers to apply the complete technical chain of three-dimensional scanning, FEM and intelligent optimization to comparative acoustic analysis of ancient and modern Chinese Suonas. It offers reliable theoretical references and reusable engineering approaches for the scientific design, quantitative performance evaluation and structural parameter optimization of traditional wind instruments.

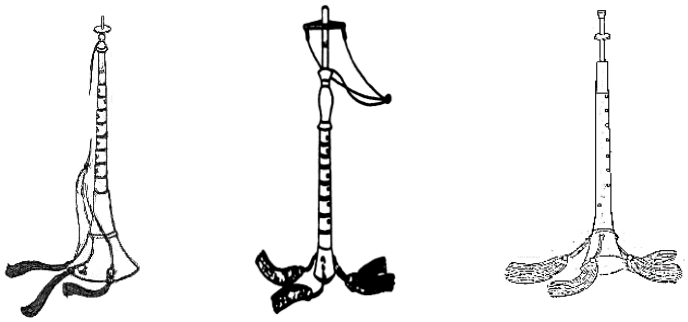
Material and methods

All methods and experimental procedures described in this work were carried out in accordance with relevant guidelines, regulations, local laboratory research rules and the principles of the Declaration of Helsinki. This study involves only routine suona performance tests and the collection of acoustic signal data of the suona instrument, with no collection of human physiological indicators, no invasive physical operations, and no interventions that might pose potential risks to participants, making it an extremely low-risk behavioral study. All experimental protocols of this study were reviewed and approved by the research administration office of North University of China, which oversees all low-risk behavioral research involving human participants within our institution. All participating performers are adults with full legal capacity who have signed written informed consent to participate in the study and allow the use of collected acoustic data. Additionally, all collected data have been fully anonymized, with no personal identifiable information of the participants recorded, in strict compliance with local data protection regulations.

Historical Records and 3D Scanning models

This work takes the Sunaiyi, a type of Suona dating back to the Qing Dynasty, and conventional modern Suonas as research subjects. As recorded in Huangchao Liqi Tushi, an official compilation of ritual artifacts from the Qing Dynasty, a collection of musical instruments was brought back from Xinjiang following the military pacification of the Hui regions during the Qianlong reign. This collection featured three double-reed wind instruments, namely the Sunaiyi, Balaman and Jinkoujiao, as illustrated in Figure 10a-c. The archival text gives thorough accounts of their physical structures and constituent materials. The Sunaiyi has a main tube made of peach wood or ebony with copper ornaments fitted at both ends. Its body tapers upward and is equipped with eight finger holes in total, seven on the front and one on the rear, while a reed mouthpiece is used for performance. The Balaman shares a similar overall structure with the Sunaiyi, yet its main tube and flared bell are carved from a single piece of wood. The Jinkoujiao is distinguished by its relatively short tube crafted from ebony. By combining historical records and unit conversions based on ancient measurement standards, the key structural parameters of the Sunaiyi are determined as follows: a total tube length of 45.25 cm, an average inner diameter of approximately 2.2 cm and a wall thickness of 5 mm, alongside eight finger holes. Its main tube is made of ebony and the bell is made of copper. Although dimensional data of the Balaman and Jinkoujiao are also available in historical documents, the Sunaiyi is selected as the representative sample of Qing-Dynasty Suonas in this study due to its well-preserved and most typical configuration. The modern Suona adopted here is a standard alto model widely used in contemporary Chinese national orchestras. It measures roughly 35 cm in total length with an average inner diameter of 2.0 cm and a wall thickness of about 4 mm. It also has seven front finger holes and one rear hole, with an ebony tube and a copper bell.

To accurately capture the true geometry of the two instruments, a non-contact 3D scanner (EinScan Pro 2X Plus) was used on the Qing Sunaiyi and modern Suona. The scanner acquires external surface data with a point-cloud accuracy of 0.1 mm, preserving key features such as the bell flare curve, tube taper, and tone hole positions, thus avoiding fitting errors of complex surfaces common in manual measurements. The non-contact method causes no physical damage to the antique Sunaiyi. The acquired point-cloud data were denoised, smoothed, and surface-reconstructed to generate high-fidelity digital models, which were then imported into COMSOL Multiphysics to build axisymmetric acoustic finite element models. This approach ensures high consistency be-tween the simulation model and the physical geometry, providing a reliable geometric basis for subsequent sound field computation and shape optimization.



(a) (b) (c)

Figure 10. Qing Dynasty double-reed instruments recorded in the Huangchao Liqi Tushi: (a) Sunaiyi; (b) Balaman; (c) Jinkoujiao.

Computer aided design

When modeling and simulating Sunaiyi and Suona in COMSOL Multiphysics, the acoustic horn shape optimization method proposed by Professor Bängtsson of Uppsala University was followed [29]. This optimization method applies to real-valued functions, as the minimum of a complex-valued function lacks a clear meaning. However, frequency-domain acoustic simulations yield a complex-valued pressure field, from which a real-valued scalar physical quantity must be constructed as the objective function. Nevertheless, any operation that maps a complex number to a real value is non-analytic, and its derivative may not be unique. By default, the gradient-based optimization solver in the Optimization Module computes the derivatives of the objective function by solving the adjoint equation, which requires special handling of the symbolic derivatives of non-analytic functions. Commonly used composite functions to obtain a real-valued objective function, such as abs(z) and conj(z), return derivative values parallel to the real axis by default. However, this property is not applicable to the adjoint method, in which the following definitions are required:

$$\frac{\mathrm{d}}{\mathrm{d}z}|z| = \frac{\overline{z}}{|z|} \tag{1}$$

$$\frac{\mathrm{d}}{\mathrm{d}z_1}(z_1\overline{z}_2) = \overline{z}_2 \tag{2}$$

$$\frac{\mathrm{d}}{\mathrm{d}z_2}(z_1\overline{z}_2)=\overline{z}_1 \tag{3}$$

By calling the built in function real-dot, which computes the real dot product of two complex vectors by taking the complex conjugate of the second vector, multiplying element wise with the first vector, and then summing the real parts of the results. If one chooses to compute p_m in the near field, or if a sufficiently large domain can be included in front of the horn to effectively measure the exterior field value at a certain point in the model, then p_m can simply be measured as the local pressure at a geometric vertex. However, to effectively optimize the directivity pattern, p_m should be defined using an integral representation of the exterior field pressure as a function of the angle relative to the axis. For a loudspeaker, this is usually the pressure or SPL calculated at 1 m. Using the definition of the Helmholtz Kirchhoff integral given in the axisymmetric formulation, the exterior field expression with the far field approximation is applied. In acoustic optimization, if one chooses to compute p_m in the near field or constructs a sufficiently large region in front of the horn to directly solve for the exterior field value at a point in the model, then p_m can simply be taken as the local pressure at that geometric vertex. However, to effectively optimize directivity, p_m should be defined using an integral expression of the exterior field pressure varying with the axial angle. For a sound emitter, this is usually the pressure or sound pressure level (SPL) calculated at 1 m. To this end, the definition of the Helmholtz Kirchhoff integral in the axisymmetric form can be adopted, and the far field approximation for the exterior field expression is used:

$$\begin{aligned} &p_{\mathrm{far}}(R)\approx-\frac{1}{2}re^{ikzZ/|R|}\int_S\left[J_0\left(\frac{krR}{|R|}\right)\left(\nabla p(r)\cdot\mathbf{n}\right)-\frac{ikp(r)}{|R|}\left(in_r\mathrm{R}J_1\left(\frac{kr\mathrm{R}}{|R|}\right)+n_zZJ_0\left(\frac{krR}{|R|}\right)\right)\right]dS \\ &\mathbf{R}=(R,Z),\quad |R|\to\infty \end{aligned} \tag{4}$$

If an infinite baffle is placed at Z = 0, the effect is the same as adding a mirror image of the horn and simultaneously removing the baffle. Moreover, if the integration surface is at the widest end of the horn in the plane of the baffle, most terms in Equation (3) cancel, leaving only:

$$p_m(\theta)=\frac{1}{L_{\mathrm{far}}}\left|\int_S J_0(kr\sin(\theta))\frac{\partial p}{\partial z}\frac{1}{2\pi}dr\right| \tag{5}$$

Where J_0 is the zero-order Bessel function of the first kind, L_{far} is the far-field calculation distance, and the angle θ relative to the axis is introduced as a parameter. Using this method, the optimization metric is based on the far-field limit of the exterior field, which is valid when the distance is greater than the Rayleigh distance $R=(1/2)Ka^2$. Multiple calculations are performed for different designs, and each design is evaluated at multiple frequencies. The sum of the objective function values for each frequency is optimized, and the parameter θ is varied to study the effect of optimizing the output at a certain angle relative to the axis on the horn shape.

To reduce computational cost while preserving simulation accuracy, the geometric symmetry of the two instruments is exploited. When building the simulation model, since both Sunaiyi and Suona are axisymmetric in shape, a half-section (2D axisymmetric) model is constructed. By revolving this half-section profile around its symmetry axis, the full 360° three-dimensional geometry of the instrument and the surrounding external sound field is generated, as illustrated in Figure 11. This approach not only significantly reduces the number of mesh elements but also ensures that the acoustic field calculations are

performed with high efficiency. The root of the pipe body is fixed as a constraint boundary to represent the structural support during playing, and a uniformly distributed pressure load is applied at the reed inlet to simulate the breath excitation exerted by the performer. This pressure loading condition mimics the unsteady airflow that drives the reed vibration, which is the primary acoustic source of the instrument [29].

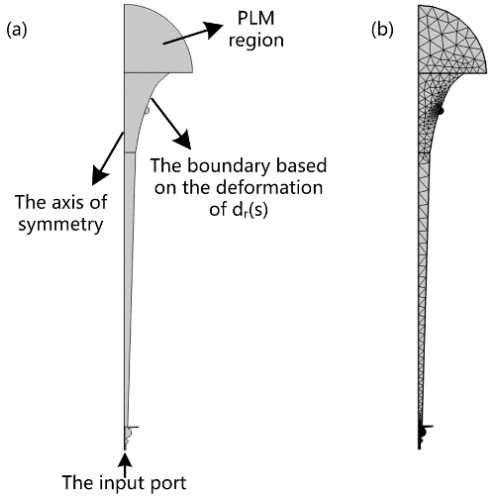


Figure 11. (a) Schematic diagram of the simulation model; (b) Mesh generation of the simulation model cross-section.

To accurately display the internal sound pressure distribution, a tetrahedral mesh was used to refine the model during meshing. The mesh size near the sound generation region was refined compared to that of the ambient field to ensure simulation accuracy. The pressure acoustics were solved in the frequency domain, and the conservation equation for porous media seepage/pressure fluctuation with external forces and wave effects was set as:

$$\nabla \cdot \left(-\frac{1}{\rho_c}\left(\nabla p_t - \mathbf{q}_d\right)\right) - \frac{k_{eq}^2 p_t}{\rho_c} = Q_m \tag{6}$$

where ∇p_t is the spatial gradient of the total pressure, $\nabla p_t - \mathbf{q}_d$ is the effective driving force after excluding external forces, and $k_{eq}^2 p_t / \rho_c$ is the wave attenuation/compressibility loss term. The solver was then configured, setting dependent variables such as material mesh displacement and sound pressure, as well as polynomial boundary conditions and scattering coefficients. Subsequently, the Multifrontal Massively Parallel sparse direct Solver (MUMPS) was used for direct solutions.

Joint optimization algorithm method

The overall working principle of the SAPSO-BCM algorithm is shown in Figure 12. The proposed algorithm integrates six core mechanisms: K-means clustering, Gaussian process (GP) surrogate modeling, LCB gradient-guided PSO evolution, periodic model management, elite opposition-based learning, and chaotic diversity resetting. The overall architecture can be divided into four functional modules: the clustering initialization module, the surrogate-assisted sub-swarm evolution module, the periodic model management module, and the chaotic diversity control module. The structure and function of each module, as well as their integration with COMSOL simulations, are described as follows.

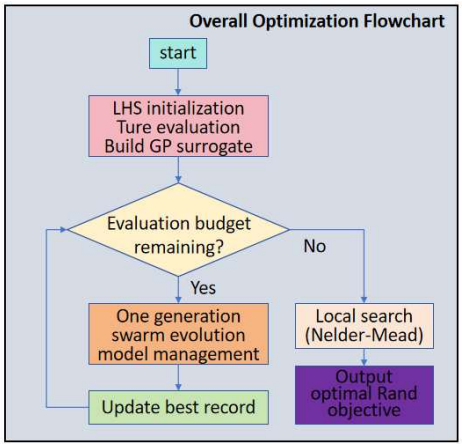


Figure 12. (a) Overall working principle diagram of the SAPSO-BCM algorithm.

This module is responsible for structurally grouping the initial candidate values (particles) of the Suona cavity curvature at the beginning of the optimization iteration. First, based on Latin Hypercube Sampling (LHS), N initial samples $\{X_i\}_{i=1}^{N}$ are generated within the preset curvature design interval $[R_{min}, R_{max}]$. COMSOL is called to perform real sound pressure level simulations, yielding the objective values $\{y_i\}_{i=1}^{N}$, which are then used to construct the initial GP surrogate model [30–31]. Subsequently, the K-means clustering algorithm is employed to partition the initial samples into K sub-swarms $\{C_k\}_{k=1}^{k}$ according to the distribution characteristics of the curvature parameter. K-means clustering is implemented by minimizing the sum of squared Euclidean distances from each sample to the center μ_k of its assigned sub-swarm [32–33], as shown in Equation (7), where $\mu_k = \frac{1}{|C_k|}\sum_{x \in C_k} x$:

$$\min_{\{C_k\}} \sum_{k=1}^{K} \sum_{x \in C_k} \|x - \mu_k\|^2 \tag{7}$$

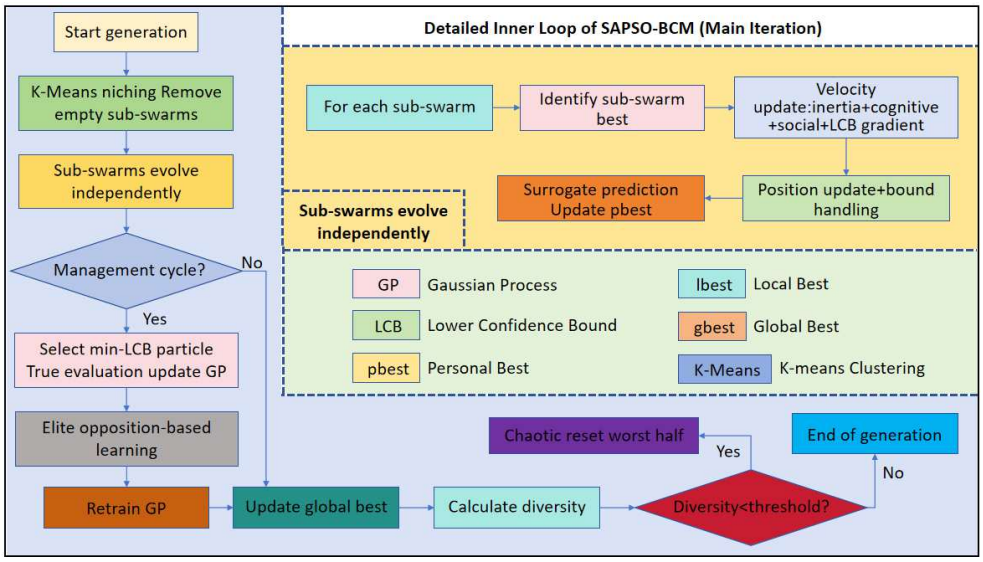


Figure 13. Single-iteration flowchart of the SAPSO-BCM algorithm and structural diagram of the surrogate-assisted sub-swarm evolution module.

After clustering is completed, empty sub-swarms containing no valid samples are removed, allowing each sub-swarm to focus on a different curvature interval for independent search. The K-means-based grouping strategy ensures that the sub-swarms are uniformly distributed in the curvature parameter space, avoids overlap of the search intervals of different sub-swarms, and enables parallel exploration across multiple intervals, thereby laying a structural foundation for the global search for the optimal curvature value. The single-iteration flowchart of the SAPSO-BCM algorithm and the structural diagram of the surrogate-assisted sub-swarm evolution module are shown in Figure 13.

During the research, the traditional PSO algorithm was modified, and an improved PSO strategy was employed to drive the independent evolution of curvature candidate values in each sub-swarm [34]. As the core execution unit of the joint simulation optimization with COMSOL, the surrogate-assisted sub-swarm evolution module first identifies, for each sub-swarm, the curvature value with the best predicted sound pressure level within the current sub-swarm (local best, lbest); it then guides the update direction of each curvature candidate value (particle). Let the position of the *i*-th particle in the *t*-th generation be $x_i^{(t)}$ (curvature value) and its velocity be $v_i^{(t)}$. The velocity update formula of the traditional PSO algorithm is given by Equation (8):

$$v_i^{(t+1)} = \omega v_i^{(t)} + c_1 r_1 \left(p_i^{(t)} - x_i^{(t)}\right) + c_2 r_2 \left(g^{(t)} - x_i^{(t)}\right) \tag{8}$$

where ω is the inertia weight, c_1 and c_2 are acceleration coefficients, $r_1, r_2 \sim U(0,1)$, $p_i^{(t)}$ is the individual historical best position (pbest), and $g^{(t)}$ is the global best position. To leverage the uncertainty information of the GP surrogate model for guiding the search, this paper introduces an LCB gradient guidance term and improves the velocity update as shown in Equation (9):

$$v_i^{(t+1)} = \omega v_i^{(t)} + c_1 r_1 \left(p_i^{(t)} - x_i^{(t)}\right) + c_2 r_2 \left(g^{(t)} - x_i^{(t)}\right) \tag{9}$$

where c_3 is the gradient guidance coefficient, and ∇LCB(x) is the gradient of the LCB acquisition function at x. The LCB function is defined in Equation (10):

$$LCB(x) = \mu(x) - \kappa\sigma(x) \tag{10}$$

where $\mu(x)$ and $\sigma(x)$ are the mean (predicted value) and standard deviation (uncertainty) of the sound pressure level predicted by the GP surrogate model at x, respectively, and κ is a weight parameter balancing exploration and exploitation. The LCB gradient ∇LCB(x) points toward regions with high uncertainty and low predicted values, guiding particles to move toward high-potential curvature intervals and avoiding the blindness of traditional PSO. The position update formula remains as given in Equation (11):

$$x_i^{(t+1)} = x_i^{(t)} + v_i^{(t+1)} \tag{11}$$

The updated curvature values are constrained within the preset design interval $[R_{min}, R_{max}]$ through boundary handling, after which the GP surrogate model predicts their sound pressure level performance and updates the individual historical best curvature value p_i of each particle. The above LCB gradient-guided velocity update mechanism effectively balances exploration and exploitation in the sound pressure level optimization. Meanwhile, the GP surrogate model replaces the vast majority of COMSOL sound pressure level simulations, greatly reducing the computational cost of the optimization process and

solving the low efficiency problem of directly calling COMSOL for iterative optimization. The structure of the surrogate-assisted sub-swarm evolution module is shown in Figure 13.

To alleviate the prediction bias drift of the GP surrogate model and enhance the utilization capability of high-quality curvature intervals, a periodic model management mechanism is embedded in the algorithm [35]. At preset management cycle nodes (every T generations), the curvature candidate value with the smallest LCB value is selected as follows:

$$x_{LCB} = arg \min_{x \in p} LCB(x) \tag{12}$$

where p is the set of all current particle positions. This point represents a curvature interval with high uncertainty and high potential. COMSOL is called to perform a real sound pressure level simulation evaluation, yielding the true objective value $f(x_{LCB})$. The newly obtained simulation data $\{x_{LCB}, f(x_{LCB})\}$ are used to retrain the GP surrogate model, correcting the prediction bias.

Statements & Declarations

Acknowledgements: The authors would like to express their gratitude to Professor Ce Gao from Shanxi University for his valuable comments on the manuscript.

Author contribution: "Conceptualization, Y.N. and P.P.; methodology, Y.N. and Z.N.; validation, P.P., Z.J. and Z.N.; investigation, Z.J.; data curation, Z.N.; writing—original draft preparation, Y.N.; writing—review and editing, P.P. and J.W.; supervision, J.W.; funding acquisition, Z.J, J.W. and Y.N. All authors have read and agreed to the published version of the manuscript." Authorship must be limited to those who have contributed substantially to the work reported."

Funding: This research was funded by National Social Science Foundation of China (No. 22BZX121); National Natural Science Foundation of China (No. 62501539); Research Project of Philosophy and Social Sciences in Higher Education Institutions of Shanxi Province (No. 2024W309).

Data availability: The data supporting the findings in this work are available from the corresponding author with a reasonable request.

Competing interests: Not applicable.

Ethical approval: All experimental operations in this study were implemented in strict accordance with local relevant laws, laboratory research guidelines and the principles of the Declaration of Helsinki. This experiment only collects acoustic signal data of suona musical instruments, without collection of human physiological indicators, invasive physical operations or any interventions that may bring potential risks to participants, and only involves routine musical performance tests with minimal risk to performers. According to local research regulatory provisions, this low-risk behavioral experiment does not require formal institutional ethical committee review. All participating performers were adults with full legal capacity, who fully understood the research content, experimental process and data usage rules before testing, and provided written informed consent to participate in this acoustic test.

References

1. Liu, W. K.; Li, S.; Park, H.S. Eighty years of the finite element method: birth, evolution, and future. Archives of Computational Methods in Engineering, 2022, 29(6): 4431-4453.

2. Keith, B.; Surowiec, T.M. Proximal Galerkin: A structure-preserving finite element method for pointwise bound constraints. Foundations of Computational Mathematics, 2026, 26(1): 385-481.
3. Mahfuz, M.; Afroj, S.; Rahman, A. Ultra-sensitive visible-IR range fiber based plasmonic sensor: a finite-element analysis and deep learning approach for RI prediction. IEEE Access. 2024, 12, 64727-64735.
4. Yokoyama, H.; Kobayashi, M.; Iida, A. Analysis of flow and acoustic radiation in reed instruments by compressible flow sim-ulation. Acoustical Science and Technology. 2020, 41(5), 739-750.
5. Yoshinaga, T.; Yokoyama, H.; Shoji, T.; Miki, A.; Iida, A. Global numerical simulation of fluid-structure-acoustic interaction in a single-reed instrument. The Journal of the Acoustical Society of America. 2021, 149(3), 1623-1632.
6. Yoshinaga, T.; Baba, R.; Yokoyama, H. Effects of two-dimensional reed oscillation on airflow and sound generation in a sin-gle-reed instrument. Computers & Fluids. 2024, 285, 106452.
7. Adachi, S. Jet oscillation model for flute-like instruments allowing overall deflection. Proceedings of Meetings on Acoustics. 2023, 52(1), 12.
8. Viala, R.; Cabaret, M.; Sedighi-Gilani, M. Effect of indented growth rings on spruce wood mechanical properties and subse-quent violin dynamics. Holzforschung: International Journal of the Biology, Chemistry, Physics, & Technology of Wood, 2024, 78(3), 189-201.
9. Francesca, T.; Luisa, V.; Gabriele, R. X-ray Computed Tomography Analysis of Historical Woodwind Instruments of the Late Eighteenth Century. Journal of Imaging. 2022, 8, 260.
10. Zhang, J.; Xiao, X.; Lee, Y.-K. The early development of music. Analysis of the Jiahu bone flutes. Antiquity. 2004, 78(302), 769-778.
11. Quile, A.; Emerit, S.; Asensi-Amorós, V. New chronometric insights into ancient Egyptian musical instruments held at the musée du louvre and the musée des beaux-arts de lyon. Radiocarbon. 2021, 63(2), 545-574.
12. Gwynne, P. Odysseus becomes first private craft to land on moon. Physics World. 2024, 37(4), 11ii.
13. Festa, G.; Pietropaolo, A.; Grazzi, F. Simultaneous and integrated neutron-based techniques for material analysis of a metallic ancient flute. Measurement Science & Technology. 2013, 24, 095601.
14. Davin, L.; Tejero, J. M.; Simmons, T. Bone aerophones from Eynan-Mallaha (Israel) indicate imitation of raptor calls by the last hunter-gatherers in the Levant. Scientific Reports. 2023, 13, 8709.
15. Wijnand, M.; Terrien, S.; Ablitzer, F.; Maugeais, S. Bifurcation analysis of a minimal model of a bowed string instrument. 11th European Nonlinear Dynamics Conference. 2024.
16. Vincent, F.; Louis, G.; Hideyuki, M.; Christophe, V.; Bruno ,C. Parameter identification of a physical model of brass instruments by constrained continuation. Acta Acustica. 2022, 6, 9.
17. Terrien, S.; Vergez, C.; Fabre, B. Emergence of quasiperiodic regimes in a neutral delay model of flute-like instruments: Influ-ence of the detuning between resonance frequencies. Journal of Computational Dynamics. 2022, 9(3), 465-482.
18. Gaudet, S.; Gauthier, C.; Sophie, Léger. The evolution of harmonic Indian musical drums: A mathematical perspective. Journal of Sound & Vibration. 2006, 291, 388-394.
19. Burred, J. J.; Robel, A.; Sikora, T. Dynamic spectral envelope modeling for timbre analysis of musical instrument sounds. IEEE Transactions on Audio Speech and Language Processing. 2010, 18(3), 663-674.
20. Brezas, S.; Katsipis, M.; Kaleris, K.; Papadaki, H.; Katerelos, D.T.G.; Papadogiannis, N.A.; Bakarezos, M.; Dimitriou, V.; Kase-louris, E. Review of Manufacturing Processes and Vibro-Acoustic Assessments of Composite and Alternative Materials for Musical Instruments. Applied. Sciences. 2024, 14, 2293.
21. Viala, R.; Placet, V.; Emmanuel, F.; Scott, C. Model based ranking of the influence of geometry and materials on the dynamical behavior of the violin highlights predominance of geometrical choices. Scientific Reports. 2024, 14, 29589.

22. James, P.; Max, Sabin. Experimental tests of free reed instrument simulations. The Journal of the Acoustical Society of America. 2023,153(3_supplement),A40-A40.
23. Bryde, P.; Mahadevan, L. Localization in musical steelpans. Proceedings of the Royal Society A: Mathematical, Physical & Engineering Sciences. 2023, 479, 20220869.
24. Takayama,S.; Tsuru, D.; Iida, A. Numerical analysis of sound radiation from a trumpet bell using boundary element method. Acoustical Science and Technology, 2018, 39(3): 251-254.
25. Chen, J.M.; Huang, C.; H., Lin.; J.W. Shape optimization of saxophone mouthpiece and bell using finite element method. Ap-plied Acoustics, 2020, 167: 107403.
26. Petiot,J.F.; Roatta, M.; Freour, Vi.; Arimoto, K. Contribution of machine learning and physics-based sound simulations for the optimization of brass instruments. Inter-noise and noise-con Congress and Conference Proceedings. 2024, 270(3), 8374-8385.
27. Wang, K.; Guo, S.; Wang, M. Finite element simulation and shape optimization of acoustic horn. Journal of Physics: Conference Series. 2021, 1944(1), 012033.
28. Barbieri, R.; Barbieri, N. Acoustic horns optimization using finite elements and genetic algorithm. Applied Acoustics. 2013, 74(3), 356-363.
29. Bängtsson, E.; Noreland, D.; Berggren, M. Shape optimization of an acoustic horn. Computer methods in applied mechanics and engineering. 2003, 192, 1533-1571.
30. Chen,X.; Mehl,C.; Faney,T.; Di, Meglio,F. Clustering-enhanced deep learning method for computation of full detailed thermo-chemical states via solver-based adaptive sampling. Energy & Fuels. 2023, 37(18), 14222-14239.
31. Safa, B.N.; Santare, M.H.; Ethier, C.R.; Elliott, D.M.Identifiability of tissue material parameters from uniaxial tests using mul-ti-start optimization. Acta Biomaterialia. 2021, 123, 197-207.
32. Wang,H.; Mo,Y. Adaptive hybrid optimization algorithm for numerical computing in engineering applications. Engineering Optimization. 2024, 57(4), 845-883.
33. Tan,Y.; Liu, S.; Zhang, L.; Song, J.; Ren, Y. The application of an improved less dung beetle optimization in the intelligent top-ological reconfiguration of ship power systems. Journal of Marine Science and Engineering. 2024, 12(10), 1843.
34. Wang, P.; Feng, Y.; Chen, Z.; Dai, Y. Study of a hull form optimization system based on a gaussian process regression algorithm and an adaptive sampling strategy, part I:single-objective optimization. Ocean Engineering. 2023, 279, 114502.
35. Xu, H.; Deng, Q.; Zhang, Z.; Lin, S. A hybrid differential evolution particle swarm optimization algorithm based on dynamic strategies. Scientific Reports. 2025, 15(1).4518.